PACKED-BED THERMAL-STORAGE SYSTEM CONFIGURATIONS FOR SHUTTLE KILN WASTE-HEAT RECOVERY

Nikolaos Georgousis[1,2,3]*, Jan Diriken[1,2], Michel Speetjens[3], Camilo Rindt[3]

[1]Flemish Institute for Technological Research (VITO), Boeretang 200, 2400 Mol, Belgium

[2]EnergyVille, Thor Park 8300, 3600 Genk, Belgium

[3]Eindhoven University of Technology, Mechanical Engineering, Energy Technology group, Groene Loper 3, 5612AE Eindhoven, The Netherlands

*Corresponding Author: nikolaos.georgousis@vito.be, n.georgousis@tue.nl

ABSTRACT

The ceramic industry, which heavily relies on non-renewable energy sources, significantly contributes to carbon dioxide emissions. In particular, periodic or shuttle kilns, used in sanitaryware production, are batch-type furnaces and are predominantly fueled by natural gas. The produced waste heat is often rejected into the environment. This study compares three distinct system configurations for waste heat recovery, which are namely: a standalone heat exchanger (HEX), crossflow or counterflow, a packed-bed thermal storage (PBTS) system for sensible heat storage, and a combination of both. A validated 1-dimensional numerical model, which solves the energy conservation equation for both solid and fluid phases is used for analyzing the PBTS system. The HEX alone recovers up to 16% of total heat input, achieving a 0.93-year payback period and a levelized cost of heat at 0.017€/kWh$_{th}$. Conversely, an optimally dimensioned PBTS system surpasses HEX efficiency, reclaiming 28.5% of the heat input. It boasts a shorter payback period (0.17-0.32 years) and lower levelized cost (0.003-0.006€/kWh$_{th}$), demonstrating its superiority in enhancing waste heat recovery in industrial settings.

1 INTRODUCTION

To meet the goals set by the "Paris Agreement", technologies for the decarbonization of the industrial sector through the recovery of produced waste heat (WH) have received significant scientific attention. Specifically, in the ceramic industry, sanitaryware production contributes to approximately 3% of the ceramic sector's total energy consumption in the EU and this energy is mainly covered by natural gas (NG) consumption (EUROPEAN COMISSION, 2007). Periodic kilns or shuttle kilns (SKs) are batch-type furnaces that operate with distinct heating and cooling trajectories and are commonly used for sanitaryware production. It has been reported that one-third of the waste heat generated in such manufacturing sites can be recovered, as currently the exhaust gas energy (around 90% of the total inlet heat) is rejected into the environment (Cuviella-Suárez *et al.*, 2021). Regarding industrial waste heat recovery (WHR), different technologies can be used, like active systems (heat pumps, power cycles) or passive systems (heat exchangers, thermal energy storage) (Miró *et al.*, 2016). WHR in the context of the ceramic industry has been considered by Kaushik and Shah (2016) where the option of recuperating waste heat of a roller kiln for tiles production for usage at the facility's dryer was examined. Mezquita *et al.* (2014) furthermore investigated the energy-saving potential of a tunnel kiln through direct gas recirculation. However, studies on WHR through thermal energy storage and specifically for the ceramic industrial sector are generally lacking in the literature.

The novelty of this research is that it focuses on industrial WHR within the context of a SK by integrating a packed-bed thermal storage system (PBTS), designed for sensible heat storage (SHS), in the production process. The PBTS system will be charged with the exhaust gas heat from the SK's cooling phase and discharged for the preheating of the combustion air during the SK's heating phase.

https://doi.org/10.52202/077185-0126

This study will compare 3 different system configurations for WHR and in all cases the WH will be reused for preheating the combustion air and thus lowering the natural gas (NG) consumption. In Section 2 the SK operation and data processing, as well as the methodologies used to analyze the counterflow and crossflow heat exchangers (HEXs) and the PBTS system, are presented. In Section 3 the performance of each WHR scenario in terms of their technical performance (WHR and thermal operation) and from a techno-economic perspective is examined. Conclusions highlight the effectiveness of the PBTS system in enhancing WHR, suggesting future research directions for optimization and broader application.

2 MATERIALS AND METHOD

In this section the SK's basic operation is discussed, emphasizing the WHR potential. Next, the processed data for a SK, based on Cuviella-Suárez *et al.* (2021), are presented. Then, the HEX and PBTS analysis methodology is explained together with underlying assumptions. For the PBTS system, a numerical model is presented, which is validated based on experimental measurements derived from a literature study.

2.1 SK Basic Operation

To analyze either the application of a HEX or a PBTS for WHR in a SK, it is necessary to study the mass and energy balance during the SK operation. Based on the study of Cuviella-Suárez *et al*. (2021) the energy balance of a SK, the NG calorific value (H_B=53.5GJ), the combustion under 10% of excess air and the stoichiometric air-to-NG mass ratio μ_{NG}=17.16 for combusting 1kg of NG, were used. The standard SK configuration includes burners combusting NG ($\dot{m}_{NG}$[kg/s]) with combustion air ($\dot{m}_{comb}$[kg/s]), along with diffusion ($\dot{m}_{dif}$[kg/s]) and injection ($\dot{m}_{inj}$[kg/s]) air to control the temperature inside the SK (T_{inside}[°C]). In total 52.798GJ of heat ($Q_{react,tot}$) are provided by NG combustion for a single operation cycle. The basic SK operation lacks WHR technology, releasing all waste heat, from both the heating (HP) and cooling phases (CP) into the environment, which are 21.350GJ and 26.855GJ respectively. Three WHR scenarios are investigated. Scenario 1 (Sc.1) involves a recuperative HEX, operating during the HP, for preheating ambient temperature (T_{amb}) combustion air ($\dot{m}_{comb}$[kg/s]) up to temperature $T_{preheated}$ by using heat from the exhaust gases ($\dot{m}_{exh}$[kg/s]) of temperature T_{exh}. Scenario 2 (Sc.2) features only a PBTS storage tank charged with heat from SK's CP, of temperature $T_{inside} = T_{exh}$, which is utilized for preheating combustion air during the next HP. Scenario 3 (Sc.3) combines both a PBTS and a recuperative HEX for maximum WHR. A schematic of the SK basic operation and the 3 WHR scenarios is provided in Figure 1.

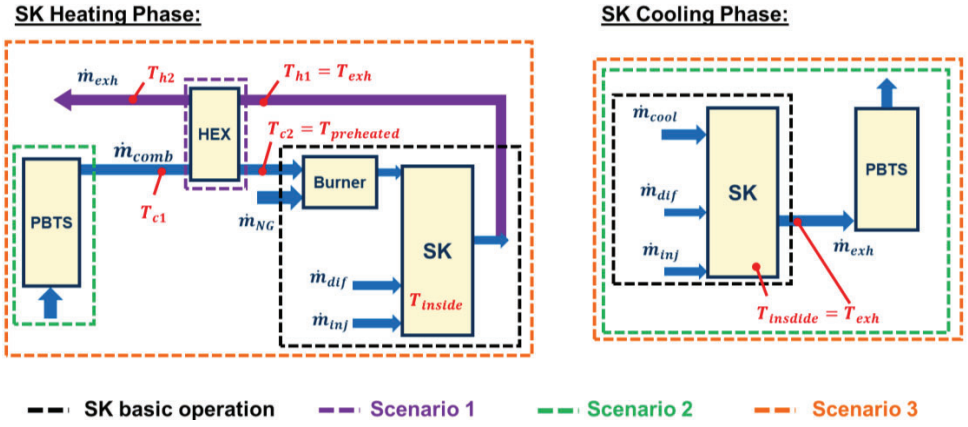

Figure 1. Schematic diagrams for the SK basic operation and the investigated 3 WHR scenarios components (indicated by a different color), during the heating (left) and cooling phase (right).

2.2 SK Data Processing

Operational data from the SK were analyzed to approximate the $\dot{m}_{comb}$, $\dot{m}_{exh}$ and exhaust gas temperature (T_{exh}[°C]) for each moment during its operation. Based on Cuviella-Suárez *et al.* (2021),

https://doi.org/10.52202/077185-0126

specific heat amounts over distinct time intervals (Δt_i[min]) for both the HP and CP, with 14 and 10 intervals respectively, were utilized. The Δt_i intervals are non-equal time steps.During the HP, given heat amounts are the combustion heat (Q_{comb}[kJ]), which is a sum of various terms like heat losses to the environment, heat absorbed by the ceramic products, diffusion, and injection heat), and exhaust gas heat (Q_{exh}[kJ]). The authors assert that Q_{comb} and Q_{exh} collectively represent the total heat input from NG consumption (Q_{react}[kJ]).

NG consumption (m_{NG}[kg]) at each stage is determined based on Q_{react} and the H_B. Based on the excess air combustion and μ_{NG} the combustion air masses (m_{comb}[kg]) are computed for every Δt_i. Injection (m_{inj}[kg]) and diffusion air masses (m_{dif}[kg]) are calculated assuming that the given heat values for Q_{dif}[kJ] and Q_{inj}[kJ] represent the heat needed for inlet masses (m_{inj} and m_{dif}) to rise from ambient temperature to the SK inside temperature (T_{inside}). T_{exh} is calculated based on the energy conservation equation at the exhaust of the SK, using the Q_{exh} and m_{exh}, where m_{exh} is the sum of m_{NG}, m_{comb}, m_{dif} and m_{inj}. For the CP, masses of cooling, injection, and diffusion air are computed similarly to the HP for m_{inj} and m_{dif}. These masses constitute CP m_{exh}, with T_{exh} assumed to be equal to T_{inside} during the CP.

The process concludes with the calculation of the required instant mass fluxes ($\dot{m}_{comb}$ and $\dot{m}_{exh}$) for 24 time moments (i_t) using backward time difference, for the non-equal time step time intervals. Also, for every Δt_i, the calculated T_{exh} values are taken for the corresponding i_t time moment. The ambient temperature is assumed T_{amb}=20°C. The calculated air and NG total masses showed an acceptable relative error compared to the values of Cuviella-Suárez *et al.* (2021), i.e. below 2%. Regarding the total combustion air the relative error was around 7%. Finally, the calculated points for the 24 i_t time moments of the SK operation, for the air and NG mass fluxes are shown in Figure 2 a. and in Figure 2 b for the temperatures inside the SK (T_{inside}) and for the exhaust gas (T_{exh}). The calculated points were interpolated using cubic-b splines to obtain all the time plots of Figure 2.

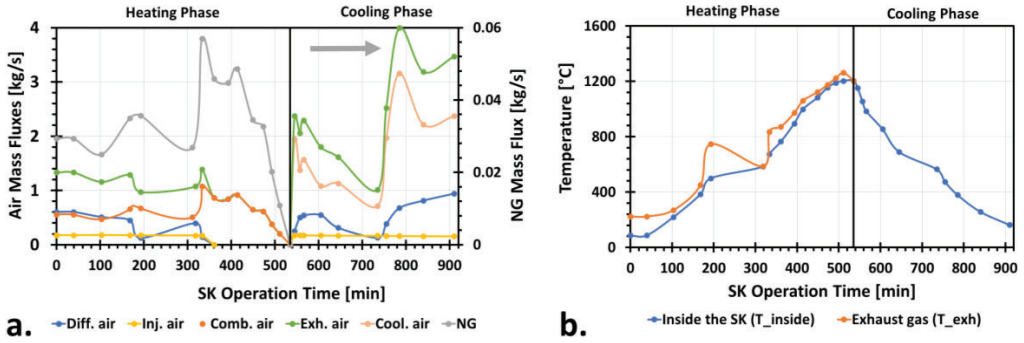

Figure 2. Calculated diagrams of **a.** air and NG mass fluxes and **b.** the temperature inside the SK (T_{inside}) and of the exhaust gas (T_{exh}), during the operation of the SK (for the cooling phase T_{exh}=T_{inside}).

2.3 HEXs Designs and Analysis

The HEX operates during the SK HP and preheats the $\dot{m}_{comb}$ (air) using the heat of $\dot{m}_{exh}$ (flue gas). The temperatures at the inlet of the HEX for the $\dot{m}_{comb}$ and $\dot{m}_{exh}$ are $T_{c1} = T_{amb}$ and $T_{h1} = T_{exh}$, while at the outlet are T_{c2} (=$T_{preheated}$) and T_{h2}, respectively (see Figure 1). Two HEX designs are considered: a crossflow, as they are used for gas-to-gas applications, and a counterflow to provide a theoretical threshold for the operation of a HEX as it can achieve maximum effectiveness. The product *UA* of HEX area (*A*) and heat-transfer coefficient (*U*) is used as the design variable and considered in the range of 1-20kW/K. Heat exchange between $\dot{m}_{exh}$ and $\dot{m}_{comb}$ is determined via the effectiveness-NTU method for both HEX designs (Komninos and Rogdakis, 2018). An operational constraint is set for the HEX, allowing their operation only as long as T_{exh} is below 1000°C (Kautz and Hansen, 2007). This means that the HEX will operate up to the time moment of 414min (T_{exh}=1056°C). For the techno-economic analysis, it is essential to calculate both the capital expenditure (*CAPEX*) and operational expenditure (*OPEX*) of the investigated components. The *CAPEX* of the HEX is also computed as a

https://doi.org/10.52202/077185-0126

function of the *UA*, with *OPEX* being estimated at 20% of *CAPEX* (Cocco and Serra, 2015; Georgousis *et al.*, 2022).

2.4 PBTS Storage Tank Geometry, Materials and Assumptions

The PBTS system under investigation consists of a cylindrical storage tank and uses air as the HTF. Spherical Electric Arc Furnace (EAF) steel slag packing elements (PEs) are used to store heat with a density of ρ_s=3430kg/m^3 and heat capacity of $c_{p,s}$=933J/kgK=const (Kocak *et al.*, 2021). The following PBTS design variables are considered constant: the aspect ratio ($a=H/D$=1), the PEs sphere diameter (d_p=1cm) and the PBTS porosity (ε=0.39). Diameter D(=H) is taken in the range of 2.25m-3.5m and the charging time (t_{ch}) varies between 150 and 375 minutes. During the PBTS charging phase (SK CP), hot exhaust air at T_{exh} of the SK charges the PBTS. The heat remains stored in the PBTS in the subsequent stand-by phase, which lasts t_{stb}=530min. The final discharging phase (SK HP) has a time duration of t_{dis}=535min. The aforementioned 3 consecutive phases correspond to 1 PBTS operational cycle, which lasts $t_{ch}+t_{stb}+t_{dis}$=24hr. Temperature T_{exh} keeps decreasing during the charging phase (Figure 2 b). For that reason, the HTF inlet in the PBTS for both the charging and discharging is from the same point (Z=0m). This way the stored heat of higher temperatures will be discharged at the beginning of the discharge phase.

The PBTS walls are considered adiabatic. Also, buoyancy-induced flow effects due to differences in air density are not considered (Schwarzmayr *et al.*, 2023). Therefore, the temperature distribution inside the PBTS can be considered 1-dimensional (1D). The calculation of the *CAPEX* includes the storage tank cost (C_{ST} [€]) and PEs specific cost (C_{PE}=80 €/tn) (Kocak *et al.*, 2021). C_{ST} is calculated using a constant cost per m^3 of the storage tank (C_V [€/m^3]). Literature provides varying C_V values and the two, lower and upper limits that were chosen are $C_{V,1}$=745€/m^3 (Cocco and Serra, 2015) and $C_{V,2}$=1580€/m^3 (Strasser and Selvam, 2014). *OPEX* was calculated as in Section 2.3.

2.5 Numerical Model for PBTS System and Validation

For analyzing the performance of the PBTS, the temperature profiles during the charging, stand-by and discharging phases for both the HTF and solid phases need to be calculated. For the computation of the temperature profiles a 2Phase–1D (2P-1D) numerical model is used, which is based on the energy conservation equation for the solid and HTF phases using a Darcy-type approach. For air-solid PBTS systems the density of the HTF (ρ_f) and the heat capacity of the solid phase (c_{ps}) are taken temperature dependent, whilst the other properties are assumed constant and computed at a reference temperature. The pressure drop is considered to have a negligible effect on the HTF density. The set of equations describing the problem consists of the mass and 2P-1D energy conservation equations (Ortega-Fernández and Rodríguez-Aseguinolaza, 2019):

HTF mass conservation:
$$\varepsilon \frac{\partial \rho_f}{\partial t} + \frac{\partial (\rho_f u_D)}{\partial x} = 0 \quad (1)$$

HTF energy conservation:
$$\varepsilon \left(\rho c_p\right)_f \frac{\partial T_f}{\partial t} + \rho_f c_{p,f} u_D \frac{\partial T_f}{\partial x} = k_{f,eff} \frac{\partial^2 T_f}{\partial x^2} + a_p h_p \left(T_s - T_f\right) \quad (2)$$

PEs energy conservation:
$$(1-\varepsilon)\rho_s \frac{\partial (c_p T)_s}{\partial t} = k_{s,eff} \frac{\partial^2 T_s}{\partial x^2} - a_p h_p \left(T_s - T_f\right) \quad (3)$$

Air state equation:
$$\rho_f = \frac{P_{ref}}{\bar{R}\, T_f} \quad (4)$$

Here u_D [m/s] is the HTF Darcy velocity, ε [-] is the porosity of the PBTS, subscripts "s" and "f" correspond to the solid PEs and HTF, respectively, T [K] is the temperature of either the PEs or HTF, $k_{f,eff}$ and $k_{s,eff}$ [W/mK] are the effective axial thermal conductivities of the 2 phases, ρ [kg/m^3] and c_p [J/kgK] are the density and specific heat, h_p [W/mK] is the convective heat transfer coefficient between the 2 phases and $a_p=6(1-\varepsilon)/d_p$ [1/m] is the "shape factor" of the PEs. The $k_{f,eff}$ and $k_{s,eff}$ are calculated based on the stagnant HTF effective conductivity (k_{stag}), while the calculation of $k_{f,eff}$ also includes the HTF thermal dispersion conductivity ($k_{f,dis}$) due to the flow through the porous structure (Ismail and Stuginsky, 1999, Yang and Nakayama, 2010). Depending on the Reynolds number of the HTF flow,

https://doi.org/10.52202/077185-0126

defined as $Re = u_D \rho_f d_p / \mu_f$ where μ_f [Pa/s] is the HTF's dynamic viscosity,different Nusselt correlations were used for the calculation of h_p (Ortega-Fernández and Rodríguez-Aseguinolaza, 2019). Relevant air properties were calculated using the Coolprop package available in Python 3.11.

In PBTS systems, during their operation, a temperature gradient zone, called "thermocline" (TC), is formed for the HTF and the PEs respectively. Inside the TC, of each phase, the temperature varies from the "high" temperature (T_H) to the "cold" temperature (T_C) level. During the (dis)charge of the PBTS the TC zones dynamically propagate inside the storage tank. The progression of the TC zones for the charging phase is illustrated in Figure 3 over a time duration Δt (the solid blue lines correspond to the HTF temperatures and the dashed yellow to the PEs). The "thermocline velocity" (u_{TC}) can be defined as the characteristic velocity at which the center of the region, enclosing both the HTF and PEs TCs, moves. The u_{TC} definition equation for incompressible HTF flow and constant properties can be found in literature (Yang and Garimella 2010). For air-solid PBTS systems where the ρ_f and $c_{p,s}$ are temperature-dependent, a first-order approximation of u_{TC} can be derived by assuming constant mass flow rate ($\dot{m}_f = \rho_f u_D A = const$), as done by Yang and Garimella (2010):

$$u_{TC} = \frac{c_{p,f}}{\varepsilon\, c_{p,f}\frac{\rho_{f,H}(T_H - T_{amb}) - \rho_{f,C}(T_C - T_{amb})}{T_H - T_C} + (1-\varepsilon)\rho_s \frac{\int_{T_C}^{T_H} c_{p,s}\, dT}{T_H - T_C}} \frac{\dot{m}_f}{A} = \frac{c_{p,f}}{\varepsilon\, \rho_{f,equiv} c_{p,f} + (1-\varepsilon)\rho_s c_{ps,equiv}} \rho_f u_D \quad (5)$$

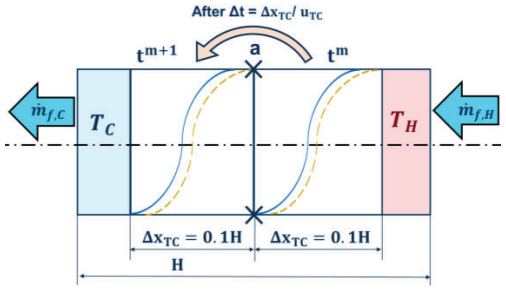

Figure 3. Schematic illustration of charging a PBTS and the thermocline progression, over a time scale $\Delta t = t^{m+1} - t^m$. HTF temperature: solid blue lines, PEs temperature: dashed yellow lines.

Here $\dot{m}_f$ [kg/s] is the HTF mass flux and A [m^2] is the PBTS cross sectional area. Based on this relationship and considering that $\rho_s \approx 10^3\, \rho_f$, it can be easily deduced that $u_{TC} \approx 10^{-3} u_D$. The distance that the TC crosses based on u_{TC} over a time duration of Δt is equal to $\Delta x_{TC} = u_{TC} \times \Delta t$. Using as a reference the temperature measurements from Esence *et al*. (2019)for charging, it can be computed that $u_{TC} = 1.29\ 10^{-4}$m/s. This means that the TC propagates by Δx_{TC}=0.31m in a 40min duration. This aligns with the experimental temperature distribution measurements (Figure 4 a.), validating Equation (5) as an initial u_{TC} estimate for PBTS systems using air/flue gas as HTF and variable $c_{p,s}$.

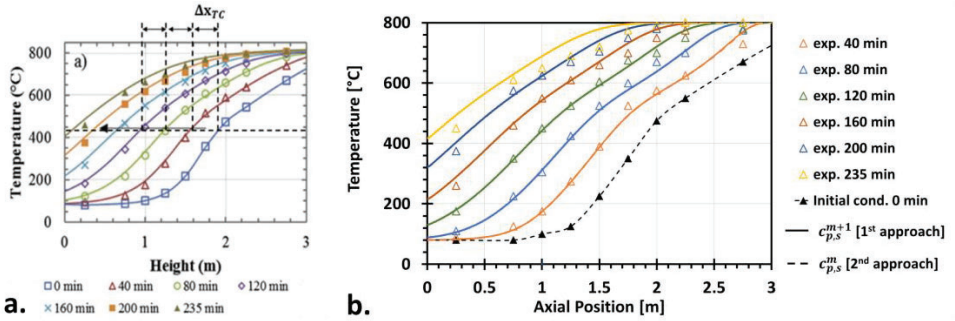

Figure 4. a. Experimental measurements of PEs temperatures for "CLAIRE" (Esence *et al*. (2019)) (only the points) and **b.** 2P-1D numerical model PEs temperature prediction for "CLAIRE" for 6 different time moments (triangle points: experimental measured solid temperatures of corresponding time moment,1st approach: solid lines, 2nd approach: dashed lines).

https://doi.org/10.52202/077185-0126

Considering the HTF mass conservation (Equation (1)) and a point in the TC region (see Figure 3) the first term T1 is of the order:

$$T1: \varepsilon \frac{\partial \rho_f}{\partial t} \approx \varepsilon \frac{\Delta \rho_f}{\Delta t} \approx \varepsilon\, u_{TC} \frac{\Delta \rho_f}{\Delta x_{TC}} \approx 10^{-4} u_D \frac{\Delta \rho_f}{\Delta x_{TC}} \tag{6}$$

The second term T2 in the HTF mass conservation (Equation (1)) is of the order:

$$\text{T2: } \frac{\partial (\rho_f u_D)}{\partial x} = u_D \frac{\partial (\rho_f)}{\partial x} + \rho_f \frac{\partial (u_D)}{\partial x} \approx u_D \frac{\Delta (\rho_f)}{\Delta x_{TC}} + \rho_f \frac{\Delta (u_D)}{\Delta x_{TC}} \tag{7}$$

It can now easily be seen from Equations (6) and (7) that T1 is negligible compared to T2, so Equation (1) becomes:

$$\frac{\partial (\rho_f u_D)}{\partial x} = 0 \Leftrightarrow \rho_f u_D = \frac{\dot{m}_f}{A} = const \tag{8}$$

By using this simplified mass conservation equation for the HTF (Equation (8)), Equation (2) and (3) can be solved independently, they are de-coupled from Equation (8). The axial dimension – height of the PBTS (H) is discretized in an equidistant grid from node $i=1$ to $i=N$, where the total number of nodes N was taken in the range of 650-1000. To discretize the 2P-1D energy conservation equations, an implicit Euler scheme was used for the time derivatives and central differences for the spatial derivatives. The time step Δt is considered between the present time moment and the previous time moment, which are indicated by the superscripts "$m+1$" and "m" respectively. Δt was taken in the range of 5-10s. For many solid phase materials, $c_{p,s}$ highly depends on the temperature. The same holds for the ρ_f of the HTF. To model the temperature dependency 2 different approaches were compared for the temperature dependent $c_{p,s}$ term of Equation (3), which are:

$$\frac{\partial (c_p T)_s}{\partial t} = \frac{\int_{T_{s,i}^m}^{T_{s,i}^{m+1}} c_{p,s} dT}{\Delta t} \approx \begin{cases} c_{p,s}^{m+1} \frac{T_{s,i}^{m+1} - T_{s,i}^m}{\Delta t} & [1^{st} approach] \\ c_{p,s}^{m} \frac{T_{s,i}^{m+1} - T_{s,i}^m}{\Delta t} & [2^{nd} approach] \end{cases} \tag{9}$$

Where i is a random node in the axial direction of the PBTS. In the 1st approach the heat capacity $c_{p,s}$ is evaluated at time level $m+1$ using an iterative process until convergence, in the 2nd approach at time level m. Regarding temperature dependency of the HTF density (ρ_f), which influences the volumetric term of Equation (2), when using the 1st approach (Equation (9)), ρ_f is evaluated at time level $m+1$ through the conducted iterative process and with the 2nd approach at time level m. With respect to the boundary conditions (BC), the inlet HTF node $i=1$ uses a known/given temperature ($T_f = T_{given}$) (Dirichlet type BC), while at the outlet node $i=N$, a 0-value Neumann type BC ($\partial T_f / \partial z = 0$) is implied. The PEs have a 0-value Neumann BC ($\partial T_s / \partial z = 0$) at the PBTS top and bottom nodes. The stand-by phase features 0-value Neumann BC for both HTF and PEs (so no heat losses to the environment).

The charging phase temperature measurements of the PBTS experimental set up called "CLAIRE" of Esence *et al.* (2019) are used for the validation of the 2P-1D numerical model. Initial conditions temperature measurements (0min-black points in Figure 4 b.) were interpolated using cubic-b splines over the PBTS height (H) assuming also that $T_{f,i}=T_{s,1}$ for $i=1,\ldots,N$ for the initial condition. The values produced from the interpolation were then used as initial condition for the 2P-1D numerical model. Figure 4 b. depicts the comparison of the PEs temperature distribution obtained from the 2P-1D numerical model with the two different approaches for the heat capacity of the PEs (Equation (9)), as well as the ρ_f, with the experimental measurement results of Esence *et al.* (2019). Six different experimental time moments are presented, ranging from 40min up to 235min. Both approaches of Equation (9) result in almost equal PEs temperature profiles between them and with good comparison to the experimental data, for most of the experimental time moments. Slight deviations with the experimental measurements can be seen only at the later stages (200min and 235min). Conclusively, the 2P-1D numerical model gives reliable results and the 2nd approach, which does not require any iteration, is adopted for the temperature dependent c_{ps} and the ρ_f.

https://doi.org/10.52202/077185-0126

2.6 Parameters and KPIs Used

The following three key performance indicators (KPIs) were used to evaluate the thermal performance of the WHR equipments (HEX and/or PBTS) and their techno-economic performance. The first KPI is the recovered waste heat for $\dot{m}_{comb}$ preheating, per SK operation cycle (WHR_{cycle}[GJ]). The other 2 KPIs are the equipment's payback period (*PBP*[years]) and levelized cost of recovered heat (*LCOH* [€/kWh$_{th}$]) (Cocco and Serra, 2015). The *PBP* was calculated based on:

$$PBP = \frac{ln\left(\frac{CF}{CF - r\,CAPEX}\right)}{ln(1+r)} \tag{10}$$

Where r is the discount rate (7%), and CF is cash flow due to the reduction of the NG consumption. The calculation of the CF is done with the equation:

$$CF = WHR_{cycle} N_{annual} C_{NG} - OPEX = WHR_{annual} C_{NG} - OPEX \tag{11}$$

Where N_{annual}=232 are the operational annual SK cycles, C_{NG}=0.0659€/kWh$_{th}$ the NG heat cost for non-household consumers in Netherlands and WHR_{annual}[GJ](=$WHR_{cycle}N_{annual}$) is waste heat that is being recovered annually. For the *LCOH* an estimation regarding the lifetime of the equipment is needed (N). A value of N=20 years was assumed. The *LCOH* was defined as:

$$LCOH = \frac{CAPEX + \sum_{n=1}^{N} \frac{OPEX}{(1+r)^n}}{\sum_{n=1}^{N} \frac{WHR_{annual}}{(1+r)^n}} \tag{12}$$

To compare the performance of the investigated HEXs with a PBTS, an optimal UA-value needs to be determined for either the crossflow or counterflow HEX. To achieve that, a multi-objective optimization criterion is used to optimize the KPIs defined above (i.e. maximize WHR_{cycle} and minimize *PBP* and *LCOH* minimize). First, the theoretical optimum design point or Ideal Point (IP) of the HEX is determined, characterized by max:WHR_{cycle}, min:*PBP* and min:*LCOH*. The optimal solution is obtained based on the minimization of a multi-objective function "F", defined as the Euclidian distance between a HEX Design Point (DP) and the IP, based on the following equation (Georgousis *et al.*, 2022):

$$F(UA) = \sqrt{\left[\frac{WHR_{cycle}(UA) - WHR_{cycle,max}}{WHR_{cycle,max} - WHR_{cycle,min}}\right]^2 + \left[\frac{PBP(UA) - PBP_{min}}{PBP_{max} - PBP_{min}}\right]^2 + \left[\frac{LCOH(UA) - LCOH_{min}}{LCOH_{max} - LCOH_{min}}\right]^2} \tag{13}$$

Where the subscripts min/max indicate the respective minimum/maximum values. An additional useful parameter is the average preheated temperature ($\bar{T}_{preh}$) of the total combustion air ($m_{comb,tot}$=19.7tn), either when using a HEX or a PBTS or both, during the SK HP. $\bar{T}_{preh}$ is defined as:

$$WHR_{cycle} = m_{comb,tot} \bar{c}_{p,air} \left(\bar{T}_{preh} - T_{amb}\right) \tag{14}$$

3 RESULTS

3.1 Scenario 1: Implementation of Crossflow and Counterflow HEX

Starting with a parametric analysis of varying the *UA* value in the range of 1-20kW/K for a crossflow and counterflow HEX, the resulting values of the WHR_{cycle}, *CAPEX*, *PBP* and *LCOH* are calculated (Figure 5). To select an optimum UA value for the crossflow and counterflow HEX, the multi-objective optimization criterion of Equation (13) is used. The optimal solution for crossflow is F=0.528, where *UA*=3.49kW/K and {WHR_{cycle}, *PBP*, *LCOH*}={8.17GJ, 1.00years, 0.0182€/kWh$_{th}$}. For the counterflow, the optimal solution is F=0.018, where *UA*=3.72kW/K and {WHR_{cycle}, *PBP*, *LCOH*}={8.54GJ, 0.93years, 0.0170€/kWh$_{th}$}.

For the optimum solutions of *UA*=3.49kW/K (crossflow) and *UA*=3.72kW/K (counterflow), the temperature diagrams of the $\dot{m}_{comb}$ and $\dot{m}_{exh}$ during the SK HP are presented in Figure 6. The diagrams show the preheated $\dot{m}_{comb}$ temperature ($T_{preheated}$=T_{c2}) and the $\dot{m}_{exh}$ inlet (T_{exh}=T_{h1}) and outlet (T_{h2})

https://doi.org/10.52202/077185-0126

temperatures during the SK HP. The T_{c2} and T_{h2} lines that correspond to the optimum *UA* counterflow HEX (darker colors) are over and below the respective T_{c2} and T_{h2} lines of the optimum *UA* crossflow HEX (lighter colors). This result is due to the better heat exchange achieved with the counterflow HEX than crossflow HEX, which also leads to higher total WHR_{cycle}.

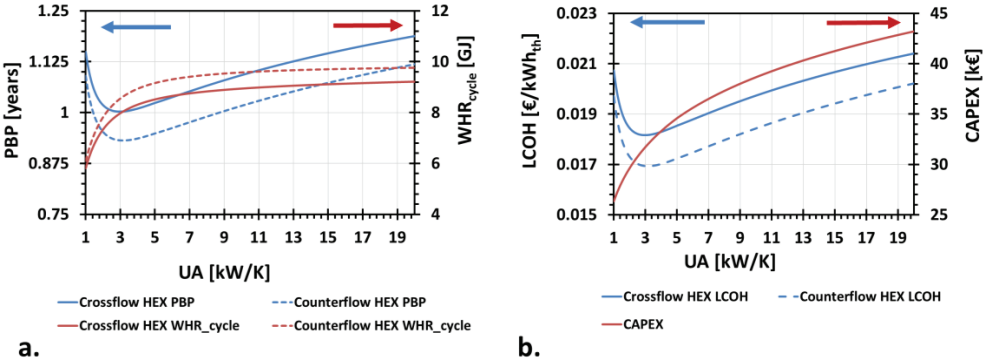

Figure 5. a. *PBP* (blue lines) and WHR_{cycle} (red lines) as function of *UA* and **b.** *LCOH* (blue lines) and *CAPEX* (red line-shared cost for both HEX types) as function of *UA* for crossflow HEX: solid lines, counterflow HEX: dashed lines.

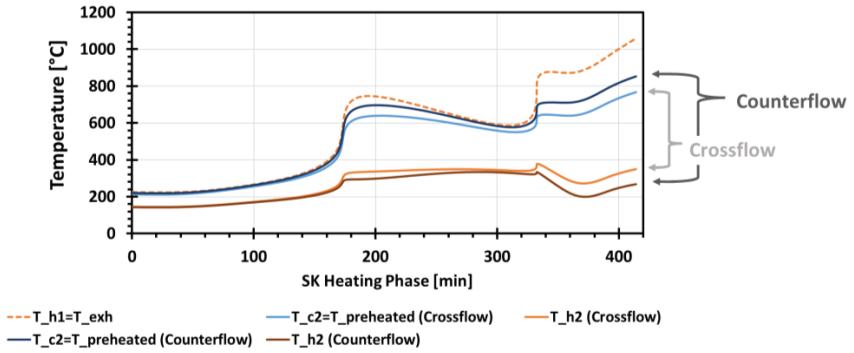

Figure 6. Temperature diagrams for optimum crossflow (*UA*=3.49kW/K) and counterflow (*UA*=3.72kW/K) HEXs. Dashed orange line: inlet temperature (T_{h1}) of $\dot{m}_{exh}$, solid orange lines: outlet temperature (T_{h2}), solid blue lines: preheated $\dot{m}_{comb}$ temperature (T_{c2}).

3.2 Scenario 2: Implementation of a PBTS System

In Sc.2 the PBTS system is charged during the SK CP by $\dot{m}_{exh}$ and discharged during the HP by $\dot{m}_{comb}$. A parametric investigation is conducted for variable storage tank diameters *D*(=*H*) ranging from 2.25-3.5m (t_{ch}=375min). Figure 7 shows the *PBP*, WH_{stored}, WHR_{cycle}, *LCOH* and *CAPEX* as a function of diameter *D*. Optimal performance is achieved at *D*=3.3m, maximizing WHR_{cycle} to 13.637GJ and minimizing *PBP* to 0.47 years (for $C_{V,1}$) and to 0.91years (for $C_{V,2}$), alongside achieving the minimum *LCOH* of 0.009 /kWh$_{th}$ (for $C_{V,1}$) and 0.017€/kWh$_{th}$ (for $C_{V,2}$). Figure 8 presents the temperature distribution of the HTF and PEs (solid and dashed lines respectively) at the end of the charging, stand-by and discharging phases inside the PBTS for 4 different diameters. The HTF and PEs temperatures are quite close at the end of the mentioned 3 operation phases.

Analysis of Figure 7 a. and Figure 8 b.-d., reveals that for PBTS systems with *D*(=*H*)>2.40m, full recovery of the stored heat (WH_{stored}) is not feasible due to the insufficient air mass available for discharge ($m_{dis,tot}$=$m_{comb,tot}$=19.7tn). This limitation is visualized through the TC region not crossing the entire PBTS height (*H*) and remaining inside the PBTS at the end of the discharge phase (Figure 8 b.-d.). This causes some stored heat to remain unused by the end of the discharge phase. Moreover, increasing *D*(=*H*) increases WH_{stored}, as more heat can be stored, yet not WHR_{cycle}, as shown in Figure 7a. Initially, as the storage tank size increases from *D*=2.25m, WHR_{cycle} rises because higher-temperature heat is stored and recovered by $\dot{m}_{comb}$ (Figure 8 a. and b.). At the optimal design point

https://doi.org/10.52202/077185-0126

(D=3.3m), most of the TC is flushed out by the end of the charging phase (Figure 8b.), and also WHR_{cycle} peaks. For D>3.3m, despite increasing WH_{stored}, WHR_{cycle} decreases (Figure 7a). Two reasons account for this. First, $m_{dis,tot}$ cannot fully discharge such PBTS storage tank sizes, as was mentioned before. Second, when D=H increases, the part of the TC stored inside the PBTS (Figure 8 c, d) and eventually discharged also increases. This leads to preheating $\dot{m}_{comb}$ at lower temperature. Especially, for D=H=3.75m, although all WH produced during the CP could be stored (WH_{stored}=26.855GJ), only 2.12GJ could be recovered, given that only part of the TC was eventually discharged.

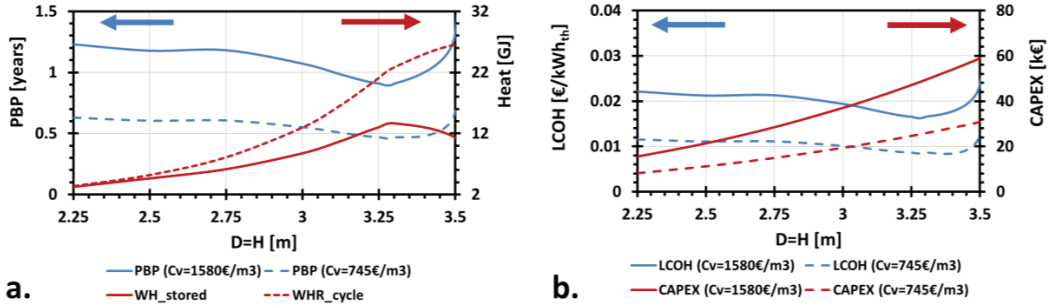

Figure 7. a. *PBP* (blue lines) for $C_{V,2}$=1580€/m^3 (solid line) and $C_{V,1}$=745€/m^3 (dashed line) and heat amounts (red lines) as a function of D and **b.** *LCOH* (blue lines) and *CAPEX* (red lines) for $C_{V,2}$=1580€/m^3 (solid lines) and $C_{V,1}$=745€/m^3 (dashed lines) as a function of D.

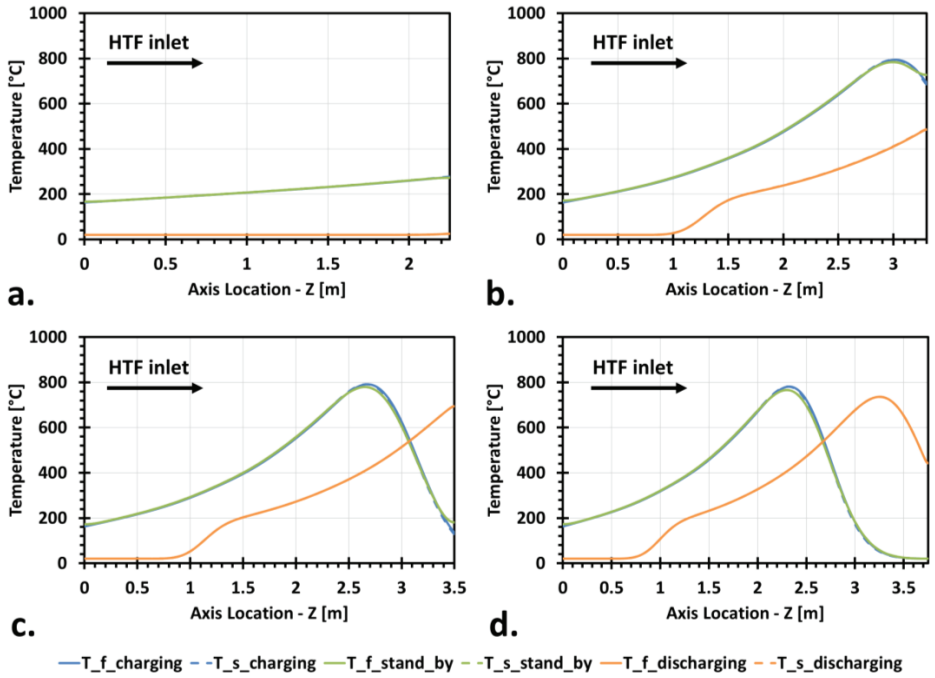

Figure 8. PBTS temperature profiles at the end of each phase for diameters (D=H) **a.** 2.25m, **b.** 3.30m, **c.** 3.50m, and **d.** 3.75m. Solid lines for HTF, dashed for PEs.

For optimal operation of the PBTS system the max:WHR_{cycle}, min:*PBP* and min:*LCOH* must be achieved and the PBTS storage tank is designed/sized so that it can be fully discharged by $\dot{m}_{comb}$. The design criterion to achieve a complete discharge of the PBTS is that the TC center fully crosses the PBTS height (H) during discharge. The average discharge thermocline velocity ($\bar{u}_{TC,dis}$) can be calculated based on Equation (5) using the average $\bar{\dot{m}}_{dis} = \bar{\dot{m}}_{comb}$=0.58kg/s based on Figure 1 a. The condition for ensuring a fully discharged PBTS is that D(=H)=$\bar{u}_{TC,dis}\ t_{dis}$ and combining this condition

https://doi.org/10.52202/077185-0126

with Equation (5) it is calculated that: D=H=2.43m. For this storage tank, the TC during the discharging can cross the PBTS height (H). The charging duration (t_{ch}) is kept as the free variable.

In Figure 9 the *PBP*, WH_{stored}, WHR_{cycle}, *LCOH* and *CAPEX* are presented as a function of t_{ch} [150-250min]. The optimum solution is for t_{ch}=212.5min, resulting in max:WHR_{cycle}=15.046GJ, min:*PBP*=0.17years (for $C_{V,1}$), 0.32years (for $C_{V,2}$) and min:*LCOH*=0.003€/kWh$_{th}$ (for $C_{V,1}$), 0.006€/kWh$_{th}$ (for $C_{V,2}$). In Figure 10 a. the temperature profiles at the end of the charging, stand-by and discharging operations for the PBTS with D=H=2.43m and t_{ch}=212.5min are presented. At the end of the discharge phase (Figure 9 a.-orange lines) the TC center has almost crossed the entire PBTS height H. In Figure 10 b. the preheated temperature during the SK HP is presented, where $\bar{T}_{preh}$=723°C.

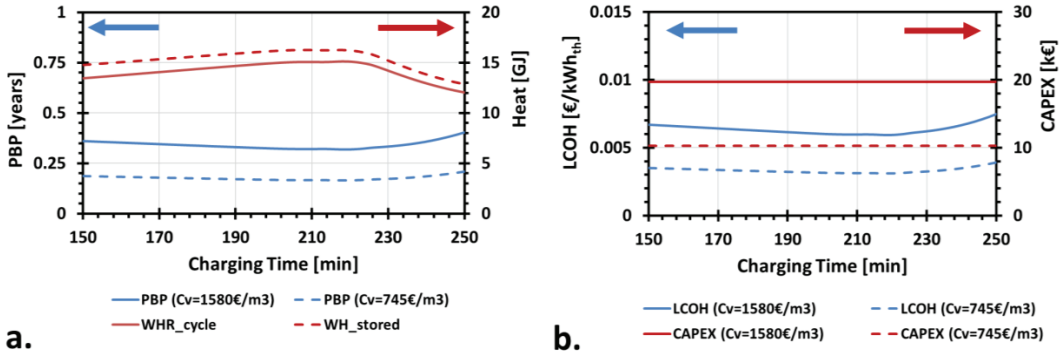

Figure 9. a. For D=H=2.43m: PBP (blue lines) ($C_{V,2}$=1580€/m^3: solid line and $C_{V,1}$=745€/m^3: dashed line) and heat amounts (red lines) as function of t_{ch} and **b.** *LCOH* (blue lines) and *CAPEX* (red lines) ($C_{V,2}$=1580€/m^3: solid lines and $C_{V,1}$=745€/m^3: dashed lines) as a function of t_{ch}.

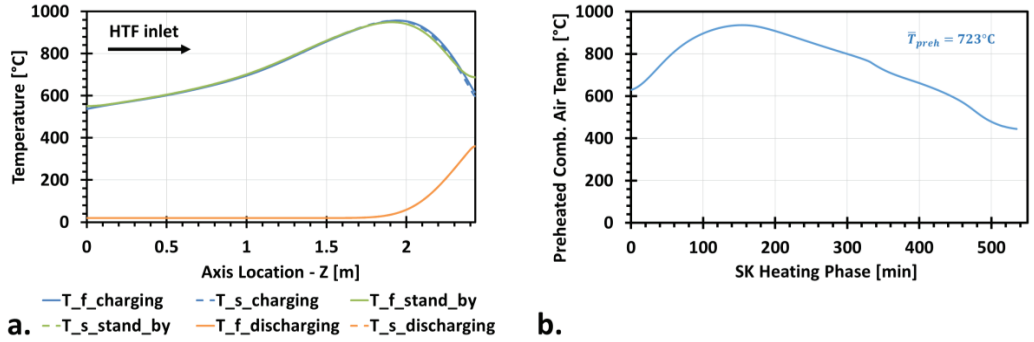

Figure 10. For the PBTS of D=H=2.43m and t_{ch}=212.5min: **a.** Temperature profiles inside the PBTS at the end of each operation phase. **b.** Preheated combustion air temperature ($T_{preheated}$) during PBTS discharge phase (SK HP).

3.3 Scenario 3: Implementation of both a PBTS System and a HEX

In Sc.3 both a cylindrical PBTS and a HEX are implemented. Regarding the PBTS system, the optimum storage tank of Sc. 2 is considered, meaning the storage tank with D=H=2.43m for t_{ch}=212.5min. Again, both a crossflow and counterflow HEX are investigated using UA as their design variable [1-20kW/K]. For the PBTS only the cost of $C_{V,2}$=1580€/m^3 is considered in Scenario 3. The total values of WHR_{cycle}, *PBP*, *LCOH* and *CAPEX* are calculated including both the PBTS and the HEX values. The contribution of the PBTS to the total WHR_{cycle} and *CAPEX* is 15.046GJ and 19.692 k€ respectively. An additional operational constraint for Sc.3 is that the HEX operates when the preheated $\dot{m}_{comb}$ temperature T_{preh} is lower than T_{exh}, so that $\dot{m}_{comb}$ can be preheated. KPIs WHR_{cycle}, *PBP*, *LCOH* and *CAPEX* as a function of UA for both HEX designs are presented in Figure 11 a. and b. To select an optimum *UA* value for the crossflow and counterflow HEX, the multi-objective optimization criterion of Equation (13) is used.

https://doi.org/10.52202/077185-0126

The resulting optimum for the crossflow HEX occurs at minimum F=0.70 for UA=2.86kW/K and corresponds with {WHR_{cycle}, PBP, $LCOH$}={15.749GJ, 0.813years, 0.0148€/kWh$_{th}$}. For the counterflow HEX, minimum F is 0.58, obtained for UA=2.89kW/K, and results in {WHR_{cycle}, PBP, $LCOH$}={15.817GJ, 0.811years, 0.0148€/kWh$_{th}$}. For the optimum UA values the $\dot{m}_{comb}$ preheated temperatures ($T_{preheated}$) as a function of SK HP time duration (535min) are presented in Figure 12 a. for the crossflow HEX and Figure 12 b. for the counterflow HEX.

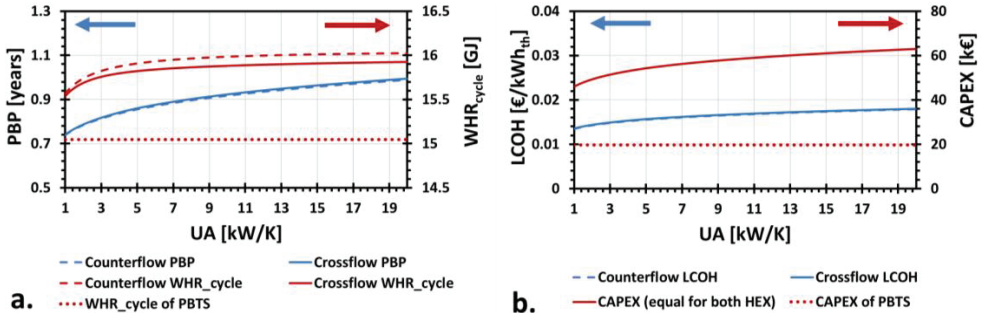

Figure 11. a. PBP (blue lines) and WHR_{cycle} (red lines) as a function of UA and **b.** $LCOH$ (blue lines) and $CAPEX$ (red line-common cost for both HEX types) as function of UA. (Crossflow HEX: solid lines, counterflow HEX: dashed lines)

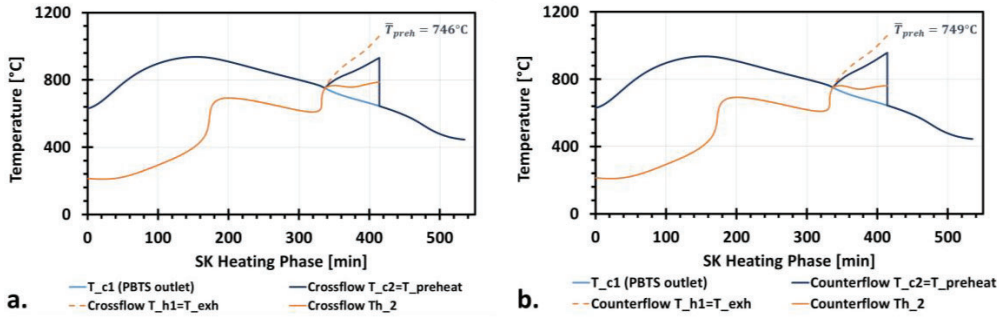

Figure 12. Preheated $\dot{m}_{comb}$ temperature diagram during the SK HP. Light blue line (T_{c1}): outlet from the PBTS, dark blue line (T_{c2}=$T_{preheated}$): final outlet from the HEX, dashed orange line: inlet temperature (T_{h1}) of $\dot{m}_{exh}$ in the HEX and the solid orange line: the outlet (T_{h2}). Diagram for optimum **a.** crossflow HEX (UA=2.86kW/K) and **b**. counterflow (UA=2.89kW/K).

4 CONCLUSIONS

This study investigates the potential usage of a PBTS system for WHR in a shuttle kiln as widely used in the ceramic industry. Three distinct system configurations for WHR, namely a standalone HEX (Scenario 1), crossflow or counterflow, a single PBTS storage tank (Scenario 2) and their combination (Scenario 3), are compared in terms of WHR_{cycle}, PBP, and $LCOH$. To this end a 2P-1D numerical model, properly adjusted and validated based on experimental measurements for air as HTF, is used. The study's key findings are the following. For Scenario 1 the optimum UA for the crossflow (UA=3.49kW/K) and counterflow (UA=3.72kW/K) HEXs leads to WHR_{cycle} of 8.17GJ and 8.54GJ, PBP of 1.0 and 0.93yrs and $LCOH$ of 0.0182€/kWh$_{th}$ and 0.0170€/kWh$_{th}$ respectively, with the counterflow outperforming the crossflow HEX at all the three KPIs used. Scenario 2 emphasizes on the proper sizing of the PBTS to preheat the total mass of the combustion air ($m_{comb,tot}$=19.7tn), through using the average thermocline velocity during the PBTS discharge phase ($\bar{u}_{TC,dis}$). Optimal PBTS performance for a storage tank that can be full discharged by $\dot{m}_{comb}$ was noted at D=H=2.43m and t_{ch}=212.5min, maximizing WHR_{cycle},=15.046GJ, minimizing PBP=0.17-0.32yrs and $LCOH$=0.003-0.006€/kWh$_{th}$ Scenario 3 combines the optimal PBTS of Scenario 2 with a HEX (crossflow or counterflow), achieving

https://doi.org/10.52202/077185-0126

the max WHR_{cycle} from all 3 scenarios, with 5% enhancement, but significant *PBP* and *LCOH* increases (154%) compared to Scenario 2 alone. Overall, of the 3 scenarios, the HEXs (Scenario 1) appear to have the worst performance, leading to the minimum WHR_{cycle} and maximum *PBP*, *LCOH*. Future research can include exploring variable PBTS aspect ratios (a), PEs diameter (d_p) and shape, utilizing multi-objective optimization for max WHR_{cycle} and min *PBP*, *LCOH*, as well as investigating WHR in other industries and either for on-site or off-site heat usage.

REFERENCES

Cocco, D., Serra, F., 2015, Performance comparison of two-tank direct and thermocline thermal energy storage systems for 1MWe class concentrating solar power plants, *Energy*, vol. 81, p. 526–536.

Cuviella-Suárez, C., Borge-Diez, D., Colmenar-Santos, A., 2021, *Green Energy and Technology Water and Energy Use in Sanitary-ware Manufacturing Using Modelling Processes for Water and Energy Accounting and Decarbonisation*, Springer Nature Switzerland AG, Cham, Switzerland, p. 1-324.

Esence, T., Desrues, T., Fourmigué, J.F., Cwicklinski, G., Bruch, A., Stutz, B., 2019, Experimental study and numerical modelling of high temperature gas/solid packed-bed heat storage systems, *Energy*, vol. 180, p. 61–78.

EUROPEAN COMISSION, *Reference Document on Best Available Techniques in the Ceramic Manufacturing Industry,* 2007, p. 1-260.

Georgousis, N., Lykas, P., Bellos, E., Tzivanidis, C., 2022, Multi-objective optimization of a solar-driven polygeneration system based on CO2 working fluid, *Energy Convers Manag*, vol. 252.

Kaushik, S., Shah, S.R., 2016, Energy utilization in ceramic tiles industries, IJARIIE, vol. 2, no. 3, p. 419-424.

Kautz, M., Hansen, U., 2007, The externally-fired gas-turbine (EFGT-Cycle) for decentralized use of biomass, *Appl Energy*, vol. 84, no. 7–8, p. 795–805.

Kocak, B., Fernandez, A.I., Paksoy, H., 2021, Benchmarking study of demolition wastes with different waste materials as sensible thermal energy storage, *Solar Energy Materials and Solar Cells*, vol. 219.

Komninos, N.P., Rogdakis, E.D., 2018, Design considerations for an Ericsson engine equipped with high-performance gas-to-gas compact heat exchanger: A numerical study, *Appl Therm Eng*, vol. 133, p. 749–763.

Mezquita, A., Boix, J., Monfort, E., Mallol, G., 2014, Energy saving in ceramic tile kilns: Cooling gas heat recovery, *Appl Therm Eng*, vol. 65, no. 1–2, p. 102–110.

Miró, L., Gasia, J., Cabeza, L.F., 2016, Thermal energy storage (TES) for industrial waste heat (IWH) recovery: A review, Applied Energy, vol. 179, p. 284-301.

Ortega-Fernández, I., Rodríguez-Aseguinolaza, J., 2019, Thermal energy storage for waste heat recovery in the steelworks: The case study of the REslag project, *Appl Energy*, vol. 237, p. 708–719.

Schwarzmayr, P., Birkelbach, F., Walter, H., Hofmann, R., 2023, Standby efficiency and thermocline degradation of a packed bed thermal energy storage: An experimental study, *Appl Energy*, vol. 337.

Strasser, M.N., Selvam, R.P., 2014, A cost and performance comparison of packed bed and structured thermocline thermal energy storage systems, *Solar Energy*, vol. 108, p. 390–402.

Yang, C., Nakayama, A., 2010, A synthesis of tortuosity and dispersion in effective thermal conductivity of porous media, *Int J Heat Mass Transf*, vol. 53, no. 15–16, p. 3222–3230.

Yang, Z., Garimella, S. V., 2010, Thermal analysis of solar thermal energy storage in a molten-salt thermocline, *Solar Energy*, vol. 84, no. 6, p. 974–985.

ACKNOWLEDGEMENT

Nikolaos Georgousis is funded by the Flemish institute for technological research (VITO).

https://doi.org/10.52202/077185-0126